

Direct observation of enhanced electron-phonon coupling in copper nanoparticles in the warm-dense matter regime

Quynh L. D. Nguyen^{1*}†, Jacopo Simoni^{2,7}, Kevin M. Dorney¹, Xun Shi¹, Jennifer L. Ellis¹, Nathan J. Brooks¹, Daniel D. Hickstein³, Amanda G. Grennell⁴, Sadegh Yazdi⁵, Eleanor E. B. Campbell⁶, Liang Z. Tan⁷, David Prendergast⁷, Jerome Daligault², Henry C. Kapteyn^{1,3}, Margaret M. Murnane¹

¹JILA, Department of Physics, University of Colorado and NIST, Boulder, Colorado 80309, USA

²Theoretical Division, Los Alamos National Laboratory, NM 87545, USA

³Kapteyn-Murnane Laboratories Inc., 4775 Walnut St #102, Boulder, CO 80301, USA

⁴Department of Chemistry, University of Colorado Boulder, CO 80309, USA

⁵Renewable and Sustainable Energy Institute, University of Colorado Boulder, CO 80309, USA

⁶EaStCHEM, School of Chemistry, Edinburgh University, David Brewster Road, Edinburgh EH9 3FJ, U.K.

⁷Molecular Foundry, Lawrence Berkeley National Laboratory, Berkeley, CA, USA.

†Present address: Stanford PULSE Institute, SLAC National Accelerator Laboratory and Stanford University, Menlo Park, CA 94025, USA.

*Email: Quynh.L.Nguyen@colorado.edu

Warm-dense matter (WDM) represents a highly-excited state that lies at the intersection of solids, plasmas, and liquids and that cannot be described by equilibrium theories. The transient nature of this state when created in a laboratory, as well as the difficulties in probing the strongly-coupled interactions between the electrons and the ions, make it challenging to develop a complete understanding of matter in this regime. In this work, by exciting isolated ~8 nm copper nanoparticles with a femtosecond laser below the ablation threshold, we create uniformly-excited WDM. We then use photoelectron spectroscopy to track the instantaneous electron temperature and directly extract the strongest electron-ion coupling observed experimentally to date. By directly comparing with state-of-the-art theories, we confirm that the superheated nanoparticles lie at the boundary between hot solids and plasmas, with associated strong electron-ion coupling. This is evidenced both by the fast energy loss of electrons to ions, as well as a strong modulation of the electron temperature by acoustic oscillations in the nanoparticle. This work demonstrates a new route for experimental exploration and theoretical validation of the exotic properties of WDM.

Introduction.

Progress in broad areas of research depends on a detailed understanding of matter under extreme conditions of temperature and pressure. The “warm dense matter” (WDM) regime corresponds to matter with a density near those of solids and a temperature from tens of K to ~10,000 K – a regime that cannot be described by equilibrium theories (1, 2). WDM lies at the heart of numerous unsolved problems in high-energy density physics (3, 4), fusion energy sciences (5), planetary sciences and stellar astrophysics (6, 7). Enabled by advances in laser technology, the last decade has seen rapid progress in the ability to make and interrogate WDM in the laboratory (8-17). These findings have shown that WDM is a very rich field of research, ripe for fundamental discoveries that highlight our understanding of strongly-interacting and highly-excited systems. Despite breakthroughs in the past decade, it still remains very challenging to directly probe the nature of the interactions within WDM, including hot electron cooling and electron-ion couplings,

particularly because of the transient nature of WDM creation in the lab, where dynamics can span from femtosecond timescales on up. This makes it difficult to validate advanced theories.

Previous studies used high-power lasers, pulsed power, and ion beams at mid and large-scale facilities to excite and probe WDM. These experiments have been limited to relatively low repetition rates (<120 Hz) (18) that influence what diagnostic measurements are actually possible. Additionally, their time resolution is often limited by streak camera diagnostics (>2 ps), which are too slow to capture the fastest electron-electron and electron-ion dynamics (19, 20). While ultrafast laser excitation at >1 kHz repetition rates can enable faster and more accurate measurements, the short penetration depth of laser light into materials, exponentially-decaying over ~ 10 nm, has represented a severe drawback to date. In a standard flat solid-target geometry, this means that the excitation and phase of the WDM changes dramatically with depth (1, 2, 21). Moreover, the high laser energy necessary to compress or superheat a sample typically causes irreversible disintegration, and requires a fresh sample for every laser shot (9, 21).

Here, we overcome these long-standing challenges by uniformly heating isolated ~ 8 nm metallic nanoparticles with a strong ultrafast laser field, where a fresh nanoparticle sample from a magnetron sputtering source is uniformly excited on every laser shot. We probe the resulting WDM dynamics using velocity-map-imaging photoelectron spectroscopy, which enables uniquely accurate measurements of this exotic state. We can directly measure the instantaneous electron temperature, and use this to accurately extract the electron-ion coupling dynamics and hot electron cooling in warm-dense matter for the first time. The electron-ion coupling values we extract are the highest observed experimentally to date. By comparing with advanced theories of highly-excited strongly-interacting matter, we find that the state of matter we produce lies at the boundary between hot solids and plasmas. This is evidenced by the fast energy loss of electrons to ions, strong modulation of the electron temperature by acoustic oscillations in the nanoparticle, and the existence of a threshold fluence associated with a change in electron-ion couplings. Our work bridges nanoscience, strong-field, and WDM physics to demonstrate a new approach for studying WDM. These results open a new avenue for experimental WDM research and inform current and future theories.

Experimental Setup

Figure 1 shows the concept, and the apparatus used for this work. A magnetron nanoparticle source produces ligand-free, isolated nanoparticles in the gas phase. The measured temperature before

laser excitation is $\sim 1,000$ K; thus, the nanoparticles start as a conventional hot solid. The source yields fresh nanoparticles that are uniform (but tunable) in size and shape (22) for every laser shot, circumventing any issues due to sample degradation by the excitation laser. The size and shape of the NPs were validated by collecting samples and then using high-resolution scanning transmission electron microscopy. The NPs are highly monodispersed and spherical with an average diameter of (8.2 ± 1.1) nm (Fig. 1c and SM). Most importantly, the size of the nanoparticles is smaller than the absorption depth (~ 13 nm) at the excitation wavelength (790 nm), enabling homogenous heating and rapid thermalization of the electrons to a hot Fermi-Dirac distribution throughout the sample, and a near-complete reduction of effects due to spatial diffusion of heat at later times.

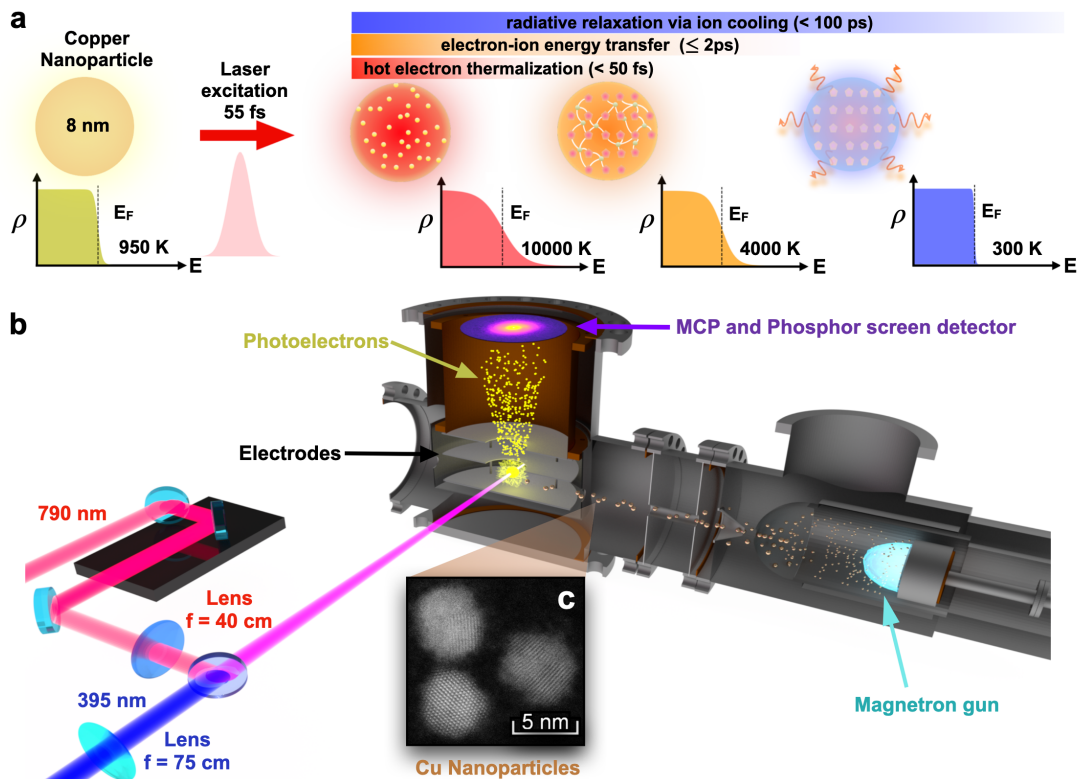


Fig. 1 | Exciting and probing dynamics of warm dense Cu nanoparticles (NPs). (a) After excitation by a 790 nm pulse, hot electrons thermalize on timescales < 50 fs. This is followed by energy transfer from the electron bath to the lattice on timescales up to 2 ps. The electron Fermi distribution (electron density (ρ) versus energy (E)) is shown, where E_F is the Fermi energy. (b) Experimental apparatus for in-vacuo ultrafast photoelectron spectroscopy of Cu NPs. A modified magnetron sputtering source produces monodisperse, highly pure Cu NPs. Subsequently, they fly through a series of differential pumping stages, which removes much of the residual generation gas and collimates the beam. They then enter the interaction region where they are excited by a 790-nm femtosecond laser pulse. A time-delayed 395-nm pulse is then used to probe the hot electron distribution as a function of pump-probe delay. The photoelectrons are guided onto a microchannel plate (MCP)-phosphor screen detector, and the resulting 2D momentum distributions are captured with a camera. (c) The lower inset shows a dark-field scanning tunneling electron microscopy image of the produced Cu NPs, confirming the high mono-dispersity, uniform crystal structure, and lack of surfactants or ligands on the nanoparticle surface.

The nanoparticles are collimated by flying through a skimmer followed by a 2-mm differential pumping aperture before entering the velocity-map-imaging (VMI) spectrometer. The nanoparticle beam is first excited with an intense 790-nm pulse ($\sim 1 \times 10^{12}$ W/cm², ~ 55 fs) to initiate dynamics, and then probed using a 395-nm ($\sim 1 \times 10^9$ W/cm², ~ 80 fs, 2nd harmonic of the fundamental laser) to ionize the particles and capture the resulting electron (and phonon) dynamics. To prevent a plasma explosion, we use laser intensities below the explosion threshold ($\sim 5 \times 10^{13}$ W/cm²) (23, 24) to uniformly heat the nanoparticle and minimize emission from charged fragments. On average, we generated a couple of electrons through multiphoton ionization per laser-particle interaction and observed no signature of an avalanche ionization process, which indicates a near-damage-threshold irradiation of solid-density materials (24). After ionization by a blue probe laser pulse, the resulting photoelectrons are guided to a microchannel plate detector, and the images are captured by a camera.

Discussion

Hot electron temperature measurement and modeling of the electron-ion coupling.

By illuminating the nanoparticles with a moderately intense laser field (10^{12} W/cm²) below the ablation threshold, electrons are excited from the occupied to unoccupied states via inverse Bremsstrahlung absorption. Very fast electron-electron scattering gives rise to a hot thermalized Fermi-Dirac distribution (within ~ 50 fs) with a very high temperature of $\sim 10,000$ K, that is initially much higher than that of the lattice ($\sim 1,000$ K, see Fig. 1a). Next, scattering of hot electrons with ions becomes the dominant relaxation mechanism, which leads to excitation of strongly coupled optical phonon modes within ~ 200 fs, followed by non-thermal melting of the lattice, depending on the pump fluence. After a few picoseconds, the ions and the electrons reach a warm thermal equilibrium of ~ 3000 K. As the particle undergoes a transformation from solid to liquid to WDM, the lattice order vanishes and the electrons become more delocalized. As shown in Figs. 3 a & c, strong acoustic phonon modes are then launched which modulate the volume of the nanoparticles, which in turn strongly modulates the electron temperature at timescales ~ 3 ps and beyond. Radiative cooling of the superheated nanoparticle will then dominate after several hundred picoseconds.

We applied two different approaches to understand the electron-ion coupling dynamics – namely a modified two-temperature model (TTM, Eqs. 1 and 2 below) (25) to extract the electron-

ion couplings, and track the energy loss both to the ions and as radiation using a phenomenological model.

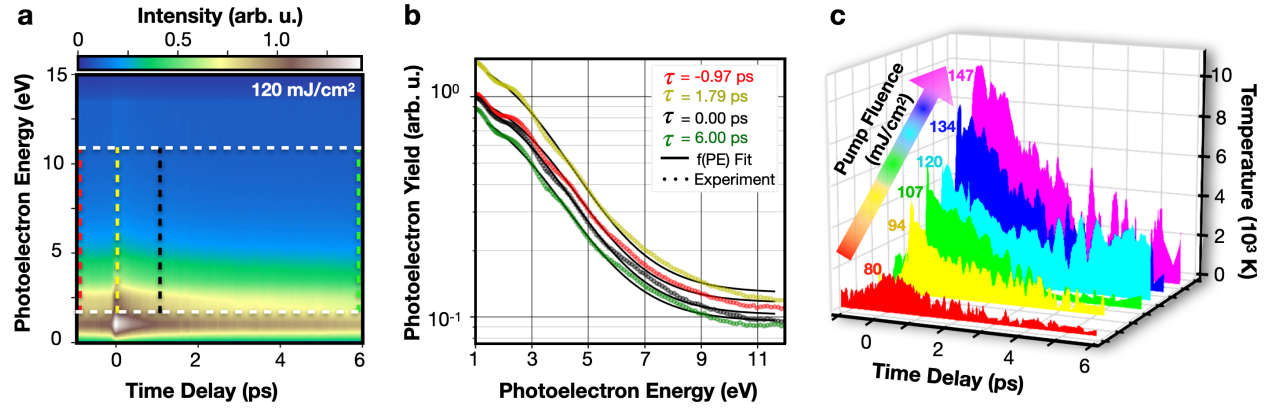


Fig. 2 | Evolution of the hot electron temperature. (a) Photoelectron (PE) energy as a function of pump-probe delay for a pump laser fluence of 120 mJ/cm². Dashed colored lines indicate the PE energy distribution curves at different time delays as shown in (b). The horizontal lines indicate the energy range for the fitting. (b) PE energy distribution curves at different time delays for the same laser intensity on a log-scale. The dashed lines show a numerical fit of the data to a thermal distribution, which is used to extract the electron temperature at each time delay (see SM). (c) Electron temperature profiles as a function of pump fluence and time delay.

First, we model the laser excitation of the nanoparticle phenomenologically using a modified two temperature model. To experimentally measure the instantaneous electron temperature, we fit the photoelectron (PE) energy distribution curves to a hot Fermi-Dirac distribution at different time delays after excitation (Figs. 2a & b). Using the same procedure, we obtained the dynamic electron temperature distributions for different laser fluences (Fig. 2 c). Next, we extracted the electron-ion coupling (G_{ei} in Eqs. 1 and 2) in the warm dense nanoplasma at varying laser fluences (F), which represents energy transfer from the electrons to the phonons/ions.

$$C_e(T_e) \frac{\partial T_e}{\partial t} = \nabla(\gamma \nabla T_e) - G_{ei}(t)(T_e - T_i) + \int dr \widetilde{p}_e \nabla \cdot \mathbf{v} + s S_{laser}(t) \quad (1)$$

$$C_i(T_i) \frac{\partial T_i}{\partial t} = \nabla(\gamma \nabla T_i) + G_{ei}(t)(T_e - T_i) \quad (2)$$

Here C_e and C_i are the electron and ion heat capacities, T_e and T_i are the electron and ion temperatures, γ is the thermal conductivity, $S_{laser}(t)$ is the laser heat source, \widetilde{p}_e is the effective electron pressure, $\nabla \cdot \mathbf{v}$ is the divergence of the velocity field in the nanoparticle, and s is the surface enhancement factor (Figs. 3a & b) (see SM). Note that many of these parameters are temperature dependent, and the ion heat capacity is kept constant at 3.5×10^6 J/Km³ based on Dulong-Petit law (26). Since the average diameter of the nanoparticles is below the absorption depth (~ 13 nm), we

assume that thermal diffusion is negligible. We refer to $G_{ei}(t)$ here as the averaged rate of energy exchange between electrons and ions, and assume the couplings are homogenous, regardless of the crystallinity of the initial ionic structure. As a first-order approximation, to minimize the number of fitting parameters when extracting G_{ei} , we initially set the electron pressure term in Eqs. 1 & 2 to zero (Figs. 3a & b). As $G_{ei}(t)$ is implicitly time-dependent because of its temperature-dependence (SM), we extract its value at peak electron temperature for comparison with other theories and experiments (Fig. 3b).

As the solid-liquid phase transition occurs, the electrons become strongly degenerate, as more d-electrons are excited and start participating in the ion-electron energy exchange, leading to an increase in the electron-ion coupling (27). Interestingly, we observe a stronger variation for G_{ei} than that previously reported for ~ 70 -nm thick Cu foil (20, 28, 29), $\sim 4 \times 10^{17}$ to 6×10^{17} W/Km³ from $T_e \sim 6,000$ to 10,000 K, which plateaus from 10,000 to 20,000 K (Fig. 3b). Our measured G_{ei} increases rapidly from $1.3 \pm 0.3 \times 10^{17}$ to $8.2 \pm 0.9 \times 10^{17}$ W/Km³ between $T_e \sim 1,800$ to 6,000 K, beyond which it plateaus (Fig. 3b). We observe an order of magnitude increase in G_{ei} at 10,000K compared to room temperature measurements for solid Cu (20, 30).

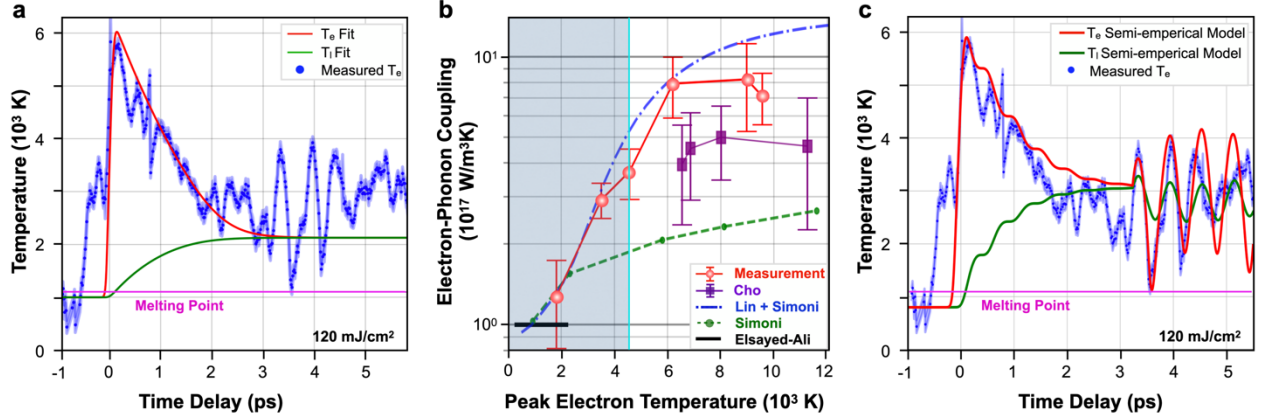


Fig. 3 | Electron-ion (phonon) couplings in warm dense matter Cu NPs. (a) Simple two-temperature fit applied to the electron temperature profile at 120 mJ/cm² to extract the corresponding electron-phonon coupling. T_e and T_i are the fittings obtained for the electron and ion temperature profiles with C_i fixed at 3.5×10^6 J/Km³. The error bars represented by the shaded blue regions indicate 99% confidence intervals. The magenta solid horizontal line indicates the melting temperature for Cu nanoparticles. (b) Electron-ion couplings obtained from fitting experimental electron temperature profiles to TTM at increasing pump intensities, and displayed as a function of the peak electron temperature of each profile. Theoretical predictions for electron-ion couplings using density of states calculated at $T_i = 950$ K temperatures using Lin and Simoni combined (blue), and Simoni (green) approaches (31). The measurements for solid Cu by Elsayed-Ali *et al.* and Cu WDM by Cho *et al.* are also shown for comparison (28, 30). The region where the quasi-equilibrium thermalized temperature falls below the bulk melting point of Cu is indicated by a the light-blue shaded region. The turquoise vertical line indicates when the lattice temperature exceeds

melting point. Experimental measurements agree with theory predicted for liquid copper where the error bars indicate 95% confidence interval. (c) The G_{ei} obtained from the fit in panel (a) and extracted acoustic modes at 1.9 THz are used in the semi-empirical two-temperature model. The red curve shows predictions from a modified two-temperature model, that includes a variation in the volume of the nanoparticles by acoustic oscillations as they transform into warm-dense nanomatter at ~ 3 ps. The frequencies of the acoustic phonons are set from the experimental data in (a), and reproduce all details of our observed electron temperature, including heating, energy loss and the large modulations observed.

We compare our measurements with the theoretical models developed by Simoni et al. (29) for bulk warm dense plasmas, which self-consistently includes the quantum, thermal, disorder, and correlations effects that coexist in this regime. We numerically evaluated G_{ei} using the Simoni approach with the electronic and ionic structures calculated with Density Functional Theory based quantum molecular dynamic simulations (31) and accurately reproduced our measurement at $T_e \sim 1,800$ K and the measured coupling for solid Cu (20, 30). Both theoretical and experimental G_{ei} increase at higher T_e ; however, with the measurements displaying a stronger temperature dependence by a factor of 4 (Fig. 3b). Meanwhile, we also computed the temperature dependence of G_{ei} using the popular model of Lin et al (32, 33). In the Lin model, G_{ei} is expressed as the product of the coupling (G_{ei}^0) at melting temperature ($T_m = 1100$ K) and a temperature-dependent correction factor that depends on the density of states (DOS) to account for the number of thermally excited electrons. While the Lin model only includes temperature variations in the DOS, Simoni et al. theory treats equally the contribution of each electron regardless of its quantum state, making it a more robust and accurate method. By setting G_{ei}^0 to the value computed using the Simoni approach (Lin+Simoni model), we obtained excellent agreement with the measurements, showing that the relaxation behavior observed before 3 ps can be well understood with existing theories for extended state electron-ion coupling.

For our case of warm dense nanoparticles, we note that additional relaxation mechanisms likely play a crucial role, that are not usually considered in existing models. These include the excitation of volume-modulated phonon modes and quantum confinement effects for a nanoparticle. The stronger agreement between theory and experiment at early times, or for lower T_e indicates that these effects become more significant as the particle undergoes a solid-liquid-WDM transformation. Hence, to understand the influence of acoustic phonon modes on the electron temperature, we introduce a pressure-volume term that accounts for the energy variation due to modulation in the volume of the nanoparticle, $\int dr p_e \nabla \cdot \mathbf{v}$ (Eqs. 1 & 2). As the particle melts and the lattice order vanishes and heats up, the electrons become significantly more delocalized

and the density of states is modulated by the excited acoustic phonons. The isolated hot nanoparticle represents an isoentropic system, where a modulation of the volume of the particle leads to a variation in the pressure of the electron density. This phenomenon results in a pronounced oscillation of the electron temperature (Figs. 3c & d), where as the entropy increases due to expansion, the electron temperature drops, and vice-versa. We note that similar oscillations have recently been observed in 2D materials at high laser fluences, where the electron temperature is modulated by the coherent phonon associated with a charge density wave distortion (34). Both are strong evidence of very strong electron-phonon/electron-ion couplings.

In addition, we note that this strong modulation of the electron temperature by the acoustic oscillations in the nanoparticle is highly fluence dependent, indicating the presence of a phase transition. For $F > F_m$, where $F_m \sim 106 \text{ mJ/cm}^2$, we observe a strong enhancement in the amplitude of the oscillations at $\sim 3 \text{ ps}$ as compared to $F < F_m$ (Figs. 4a & b). This is likely due to the change in the volume of the nanoparticles as the lattice order vanishes (12, 14). This causes electrons to be more delocalized and the electron density varies strongly as the particle undergoes a solid-liquid-WDM transformation. Associated with the strong modulations of the electronic temperature are significant enhancements of the electron-ion coupling, arising from temperature variations in the DOS in the Lin+Simoni model. We account for prominent-amplitude acoustic phonons ($\sim 1.9 \text{ THz}$) exhibited in the electron temperature profile using the pressure-volume term implemented in the TTM model (Figs. 3a & c). These surprising phenomena may be uniquely associated with the intrinsic properties of isolated nanoparticles, where hot electrons are confined more effectively than in a flat-target geometry, and thus have not been previously observed (12, 20, 28, 29).

Electron-ion coupling dynamics.

Next, we applied a phenomenological exponential model convolved with the instrument response function to further understand coupling to the ions as well as radiation loss (refer to SI). Figure 4 shows the extracted $1/e$ time constants of electron-ion energy transfer (τ_{ei}), where $F < F_m$ (equivalently $T_l < T_m$) is the hot solid regime. The solid-liquid-WDM phase transformation leads to modifications in the density of states (DOS) and the electron heat capacity that influence the electron-ion cooling rates. At higher T_e , the temperature dependence of C_e reduces the electron-ion thermalization rate (35) while G_{ei} exhibits an opposite effect. Within the solid and liquid regimes, we observe a decrease in the electron-ion thermalization rate with increasing T_e (i.e.

increase in τ_{ei}), which indicates that the C_e effect dominates over the G_{ei} influence (Fig. 4b). However, at the solid-liquid-WDM transformation at F_m (equivalently $T_e \sim 5,000$ K) (Figs. 3b & 4b), C_e drops, which enhances the electron-ion thermalization rate. Thus, τ_{ei} exhibits a sudden drop, or a kink, at F_m that signals the phase transition. Our extracted τ_{ei} for the WD nanomatter at $T_e \sim 10,000$ K (1.5 ± 0.1 ps) is ~ 1.3 ps shorter than previously measured for flat-target Cu WDM (2.8 ± 0.4 ps) (28). This is likely due to the additional thermalization mechanisms that we observed for the warm-dense nanomatter. For example, the acoustic phonon modes leading to a time variation in the nanoparticle volume as it transforms into WDM (Figs. 4a & b) can speed up energy redistribution in the superheated nanoparticles. This effect has also been theoretically predicted to accelerate the electron-ion heat exchange process in WD plasmas (36, 37) and observed for semiconductors and semimetals (38-40).

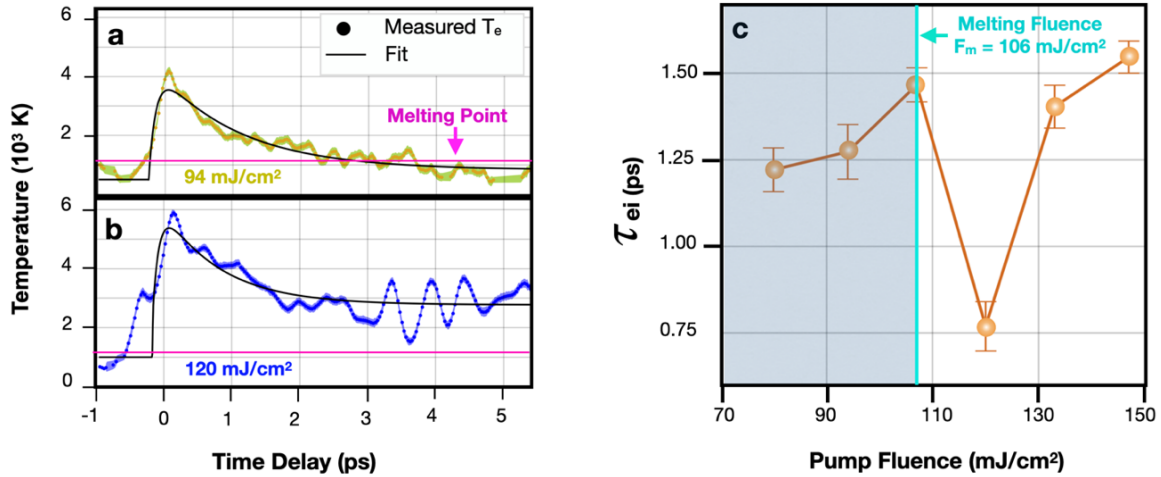


Fig. 4 | Hot electron dynamics of Cu Nanoparticles. Extracted temporal evolution of electron temperature at pump fluences of (a) 94 mJ/cm² and (b) 120 mJ/cm², below and above the melting fluence. The solid black lines represent the double exponential convolved with the instrument response function of 99 ± 1 fs to determine the 1/e time constants for the electron-ion thermalizations. The magenta solid horizontal line indicates the melting temperature for Cu nanoparticles. The extracted time constants are shown in (c) for the electron-phonon energy transfer processes. The solid vertical turquoise line indicates the fluence where the electron-ion bath thermalize to a temperature above the bulk melting point. The error bars are 95% confidence intervals. The turquoise vertical line at 106 mJ/cm² indicates the laser fluence where the lattice exceeds the bulk melting point post-electron-ion thermalization.

In conclusion, we have developed a unique method for probing the strong electron-ion coupling that is present in uniformly-excited warm dense matter – in this case laser-excited Cu nanoparticles. By tracking the instantaneous hot electron temperature, we can precisely extract the electron-ion coupling, which attains a maximal value of $8.2 \pm 0.9 \times 10^{17}$ W/Km³ over the transient electron temperature range from 1,800 to 10,000 K. This is higher than previously observed

experimentally and on the high end of *ab initio* theories. In addition, the acoustic phonons launched by impulsive laser heating also induce a very strong modulation of the electron temperature on picosecond timescales, once the nanoparticle has undergone a phase transition into the warm dense matter regime and the lattice order has melted. This study defines a generalizable approach to the study of WDM phenomena across a wide range of different materials via the generation of isolated nanoparticles. Finally, our direct measurements of electron energy loss can validate advanced theories that can include effects such as the effect of particle-size, laser excitation parameters and strongly-coupled phonon modes on the electron-ion coupling and cooling pathways.

References:

1. At the Frontier of Scientific Discovery, U.S. DOE Report of the Panel on Frontiers of Plasma Science, 2017.
2. R. W. Lee, Finite temperature dense matter studies on next-generation light sources. *J. Opt. Soc. Am. B* **20**, 4 (2003)
3. S. Lebedev, *High Energy Density Laboratory Astrophysics* (Springer, 2007).
4. S. H. Glenzer et al., Symmetric inertial confinement fusion implosions at ultra-high laser energies. *Science* **327**, 1228–1231 (2010).
5. J. H. Nguyen et al., Melting of iron at the physical conditions of the Earth’s core. *Nature* **427**, 339 (2004).
6. T. Guillot., “Interiors of giant planets inside and outside the solar system”, *Science* **286**, 72 (1999).
7. Heinonen, R. A. "Diffusion coefficients in the envelopes of white dwarfs", *The Astrophysical J.* **896**:2 (2020).
8. R. Ernstorfer et al., The formation of warm dense matter: experimental evidence for electronic bond hardening in gold. *Science* **323**, 1033–1037 (2009).
9. B. Nagler et al., Turning solid aluminium transparent by intense soft X-ray photoionization. *Nat. Phys.* **5**, 693–696 (2009).
10. S. M. Vinko et al., Creation and diagnosis of a solid-density plasma with an X-ray free-electron laser. *Nature* **482**, 59–62 (2012).
11. R. F. Fäustline et al., Observation of Ultrafast Nonequilibrium Collective Dynamics in Warm Dense Hydrogen. *Phys. Rev. Lett.* **104**, 125002 (2010).
12. B. Mahieu et al., Probing warm dense matter using femtosecond X-ray absorption spectroscopy with a laser-produced betatron source. *Nat. Comm.* **9**, 3276 (2018).
13. K. Falk et al., "Experimental methods for warm dense matter research", *High Power Laser Science and Engineering* **6**, 59 (2018).
14. L. B. Fletcher et al., "Ultrabright X-ray laser scattering for dynamic warm dense matter physics" *Nat. Photon.* **9**, 274–279 (2015).
15. A. C. Hayes et al., "Plasma stopping-power measurements reveal transition from non-degenerate to degenerate plasmas" *Nat. Phys.* **16**, 432–437 (2020).
16. A.B. Zylstra et al., “Measurement of charged-particle stopping in warm dense matter”, *Phys. Rev. Lett.* **114**, 215002 (2015).
17. F. Graziani, M. P. Desjarlais, R. Redmer, S. B. Trickey. editors, *Frontiers and Challenges in Warm Dense Matter* (Springer-Verlag, Heidelberg, 2014).
18. S. H. Glenzer, Matter under extreme conditions experiments at the Linac Coherent Light Source. *J. Phys. B: At. Mol. Opt. Phys.* **49**, 092001 (2016)

19. J. Feng et al., A grazing incidence x-ray streak camera for ultrafast, single-shot measurements. *Appl. Phys. Lett.* **96**, 134102 (2010)
20. B. I. Cho et al., Electronic Structure of Warm Dense Copper Studied by Ultrafast X-ray Absorption Spectroscopy. *Phys. Rev. Lett.* **106**, 167601 (2011).
21. F. Dorchies et al., Unraveling the Solid-Liquid-Vapor phase transition dynamics at the atomic level with ultrafast X-ray absorption near-edge spectroscopy. *Phys. Rev. Lett.* **107**, 245006 (2011)
22. I. Barke et al. The 3D-architecture of individual free silver nanoparticles captured by X-ray scattering. *Nat. Comm.* **6**, 6187 (2015).
23. D. D. Hickstein et al., Observation and control of shock waves in individual nanoplasmas. *Phys. Rev. Lett.* **112**, 115004 (2014).
24. D. D. Hickstein et al., Mapping Nanoscale absorption of femtosecond laser pulses using plasma explosion imaging. *ACS nano* **8**, 9, 8810-8818 (2014).
25. S. I. Anisimov et al., Electron emission from metal surfaces exposed to ultrashort laser pulses. *Zh. Eksp. Teor. Fiz.* **66**, 375–377 (1974).
26. American Institute of Physics Handbook, edited by D. E. Grady (McGraw-Hill, New York, 1972), 3rd ed.
27. J. Simoni et al., First-Principles Determination of Electron-Ion Couplings in the Warm Dense Matter Regime. *Phys. Rev. Lett.* **122**, 205001 (2019).
28. B. I. Cho et al., Measurement of Electron-Ion Relaxation in Warm Dense Copper. *Sci. Rep.* **6**, 18843 (2016).
29. N. Jourdain et al. Electron-ion thermal equilibration dynamics in femtosecond heated warm dense copper. *Phys. Rev. B* **97**, 075148 (2018)
30. H. E. Elsayed-Ali et al., Time-resolved observation of electron-phonon relaxation in copper. *Phys. Rev. Lett.* **58**, 1212 (1987).
31. J. Simoni et al., Calculation of electron-ion temperature equilibration rates and friction coefficients in plasmas and liquid metals using quantum molecular dynamics. *Phys. Rev. E* **101**, 013205 (2020).
32. Z. Lin et al. Electron-phonon coupling and electron heat capacity of metals under conditions of strong electron-phonon nonequilibrium. *Phys. Rev. B* **77**, 075133 (2008).
33. X. Y. Wang et al., Time-resolved electron-temperature measurement in a highly excited gold target using femtosecond thermionic emission. *Phys. Rev. B* **50**, 8016 (1994).
34. Zhang, Y.; Shi, X.; You, W.; et al. Coherent modulation of the electron temperature and electron-phonon couplings in a 2D material. *PNAS* **117** (16) 8788-8793 (2020).
35. M. Z. Mo et al. Determination of the electron-lattice coupling strength of copper with ultrafast MeV electron diffraction. *Rev. Sci. Instrum.* **89**, 10C108 (2018)
36. M. W. C. Dharma-wardana. Nature of Coupled-Mode Contributions to Hot-Electron Relaxation in Semiconductors. *Phys. Rev. Lett.* **66**, 2 (1990)
37. J. Vorberger. Coupled mode effects on energy transfer in weakly coupled, two-temperature plasmas. *Phys. Plasmas* **16**, 082702 (2009)
38. A. Rousse et al. Non-thermal melting in semiconductors measured at femtosecond resolution. *Nature* **410**, 65-68 (2001)
39. Von der Linde, D et al. ‘Ultrafast’ extended to X-rays: Femtosecond time-resolved X-ray diffraction. *Z. Phys. Chem.* **215**, 1527-1541 (2001)
40. T. Kampfrath. Strongly Coupled Optical Phonons in the Ultrafast Dynamics of the Electronic Energy and Current Relaxation in Graphite. *Phys. Rev. Lett.* **95**, 187403 (2005)
41. H. Haberland et al. Filling of micron-sized contact holes with copper by energetic cluster impact. *J. Vac. Sci. Technol. A* **12**, 2925–2930 (1994).
42. A. T. Eppink, D. H. Parker. Velocity map imaging of ions and electrons using electrostatic lenses: Application in photoelectron and photofragment ion imaging of molecular oxygen. *Rev. of Sci. Instr.* **68**, 3477 (1997).
43. D. H., Parker, A. T. J. B. Eppink. Photoelectron and photofragment velocity map imaging of state-selected molecular oxygen dissociation/ionization dynamics. *J. Chem. Phys.* **107**, 2357 (1997).

44. E. W. Hansen, P.-L. Law. Recursive methods for computing the Abel transform and its inverse. *J. Opt. Soc. Am. A*, **2**, 510-520 (1985).
45. E. W. Hansen. Fast Hankel transform algorithm. *IEEE Trans. Acoust. Speech Signal Proc.* 1985, **33**, 666-671
46. C. C. Blackstone. Photoelectron angular distributions in detachment from polarized d-like states: the case of HO_2^- . *Mol. Phys.* **119**, e1831636 (2020).
47. Multiphysics, C. (1998). Introduction to COMSOL multiphysics extregistered. *COMSOL Multiphysics, Burlington, MA, Accessed Feb, 9, 2018*
48. P. Giannozzi *et al.*, QUANTUM ESPRESSO: a modular and open-source software project for quantum simulations of materials. *J.Phys.:Condens.Matter* **21**, 395502 (2009).
49. P. Giannozzi *et al.*, Advanced capabilities for materials modelling with Quantum ESPRESSO. *J.Phys.:Condens.Matter* **29**, 465901 (2017).
50. I. T. Todorov *et al.* DL_POLY_3: new dimensions in molecular dynamics simulations via massive parallelism, *Journal of Materials Chemistry*, **16**, 1911 (2006).
51. C. Chen *et al.* In-situ high-resolution transmission electron microscopy investigation of overheating of Cu nanoparticles. *Sci. Rep.* **6**, 19545 (2016)

Author Contributions: Q.L.D.N., D.D.H., K.M.D., J.L.E., H.C.K., M.M.M. designed the experiment. Q.L.D.N., K.M.D., J.L.E. and N.J.B., acquired the experimental data. Q.L.D.N., A.N.G., and S.Y. conducted the TEM measurements. Q.L.D.N. and K.M.D. analyzed the data. N.J.B. performed finite element analysis simulations. J.S. and J.D. performed theoretical analysis. Q.L.D.N., J.S., J.D., H.C.K., and M.M.M. wrote the manuscript. All authors contributed to discussions and provided comments to the manuscript.

Funding: Q.L.D.N., K.M.D., J.L.E, N.J.B., H.C.K., M.M.M. acknowledge support from the DOE Office of Basic Energy Sciences (AMOS program). Q.L.D.N., J.L.E., N.J.B., and A.N.G. were also supported by the National Science Foundation Graduate Research Fellowship (DGE-1144083). S.Y. acknowledges support from the Facility for Electron Microscopy of Materials at the CU Boulder (CU FEMM). E.E.B.C acknowledges support of a JILA visiting fellowship. J.S. and J.D. were supported by the Laboratory Directed Research and Development program of Los Alamos National Laboratory under project number 20200074ER. This research used resources of the National Energy Research Scientific Computing Center, a DOE Office of Science User Facility supported by the Office of Science of the U.S. Department of Energy under Contract No. DE-AC02-05CH11231. We thank Joshua Knobloch and Christian Gentry for fruitful discussions.

Competing interests: The authors declare no competing interests.

Data and materials availability: All data are available in the main text or the supplementary materials